# Highly dispersed PdS preferably anchored on $In_2S_3$ of $MnS/In_2S_3$ composite for effective and stable hydrogen production from $H_2S$

Yi Li[ab], Shan Yu*[ab], Dmitry E. Doronkin[c], Shiqian Wei[ab], Meng Dan[ab], Fan Wu[ab], Liqun Ye[d], Jan-Dierk Grunwaldt[c], Ying Zhou*[ab]

As an important byproduct during natural gas exploitation, green utilization of hydrogen sulfide ($H_2S$) by photocatalysis has offered us the possibility for production of clean hydrogen ($H_2$) from $H_2S$ with low energy consumption. In this work, we have successfully introduced well-dispersed palladium sulfide (PdS) which is preferably loaded on $In_2S_3$ of $MnS/In_2S_3$ composite for improved photocatalytic hydrogen evolution from $H_2S$ aqueous solution. In contrast to binary $MnS/In_2S_3$, ternary $MnS/In_2S_3$/PdS has exhibited a remarkable and stable hydrogen production rate of 22.7 mmol $g^{-1}$ $h^{-1}$ with an apparent quantum yield of 34 % at around 395 nm. A comprehensive structure characterization of the ternary composite including scanning transmission electron microscopy (STEM) and X-ray absorption spectroscopy (XAS) in combination with theoretical calculations confirm the good dispersion of PdS in the composite. Moreover, we discovered that PdS preferably interact with $In_2S_3$ rather than MnS in the composite through Pd-S-In bond on the interface of the two. Photoluminescence (PL) spectra, surface photovoltage (SPV) spectra together with transient photocurrent and electrochemical impedance spectra (EIS) demonstrate the advantage of PdS for promoting the charge separation. Due to the corrosion-resistant nature of PdS in $H_2S$-rich reaction media, $MnS/In_2S_3$/PdS present good stability as well. This work sheds light on the positive effect on the enhanced activity and stability of the corresponding system resulting from the preferable anchoring of highly dispersed PdS on $In_2S_3$ in the composite by chemical Pd-S-In bond. Not only the high dispersion but also the preferable anchoring of the cocatalyst in the composite could hence inspire people for more rational designs of ternary composite in future.

## Introduction

Hydrogen sulfide ($H_2S$), largely produced in oil and gas exploitation, has attracted great attention focused on its efficient removal because of its corrosive properties and high toxicity ($LC_{50}$ approximately 500 ppm).[1-3] $H_2S$ is largely produced in the hydrodesulfurization process of heavy oil during exploitation, in which hydrogen ($H_2$) is consumed.[4] On the other hand, from the standpoint of sustainable energy production, $H_2S$ is regarded as a good resource resulting from its special elemental composition. In terms of $H_2S$ conversion, various techniques have been proposed. Traditionally, $H_2S$ was handled in industry with Claus process,[5] in which $H_2S$ was converted to sulfur and $H_2O$. But one should be aware of the potential of hydrogen contained in $H_2S$ as well. Accordingly, other methods that focus on collection of $H_2$ from $H_2S$ have been developed.[6-10] Among them, photocatalysis is regarded as a promising technique due to its potential for direct conversion of solar energy into clean fuels.[11-19] Using photocatalysis one can recover the consumed $H_2$ and recycle it back in the hydrodesulfurization. Notably, photocatalytic hydrogen evolution from $H_2S$ is thermodynamically more favorable compared to traditional photocatalytic $H_2O$ splitting: $\Delta G$ for $H_2S$ splitting (39.4 kJ $mol^{-1}$) is far less than that for water splitting (284.7 kJ $mol^{-1}$).[20] Hence, there is a broader choice for the photocatalysts which could promote $H_2S$ decomposition.

Among various kinds of photocatalysts, metal sulfides exhibit many advantages due to their suitable band structure and strong visible-light absorption. Many research works focused on sulfides such as CdS,[21-24] ZnS,[25] $CuInS_2$[26] have been reported; meanwhile, the development of other metal sulfides is necessary.[27] In our previous work,[28] we discovered that $MnS/In_2S_3$ composite is an effective photocatalyst for hydrogen evolution from $H_2S$ in the visible light region. Nevertheless, the catalytic activity of $MnS/In_2S_3$ composite is insufficient for practical application and further optimization is required. Introduction of noble metal cocatalyst such as Pt[29] and Pd[30, 31] for promotion of charge separation efficiency as well as surface reaction kinetics is a widely recognized method for improving the photocatalytic efficiency. However, the poisoning effect of $H_2S$, which can inhibit the activity of noble metals,[32-34] makes it difficult to directly utilize Pt or Pd in the $H_2S$ related research. To address this issue, noble metal sulfides were used instead due to their more resistant properties to the harsh sulfidizing environment compared to pure noble metals. Among them, palladium sulfide (PdS) has been reported to be a good cocatalyst when combined with CdS,[35] $Zn_{0.5}Cd_{0.5}S$[36] and ZnS-$CuInS_2$.[37]

Nevertheless, traditional cocatalysts are prone to agglomeration during the activation and photocatalysis[38, 39] decreasing the atomic efficiency of earth-scarce palladium. To better exploit palladium, the size of cocatalyst particles needs to be decreased to clusters or even to single atoms,[40, 41] maximizing the fraction of accessible active sites during

photocatalysis. More importantly, when the size of the cocatalyst particles is small enough, additional interaction between the cocatalyst and the substrate has been reported in a series of works.[42] For example, abundant Pt-S bonds are formed between unsaturated sulfur atoms from CdS and isolated platinum atoms.[43] It was also found that Pd atom strongly interacts with $TiO_2$ to maintain its stability as well.[44] Such interaction plays a crucial role in preventing the sintering of the cotatalyst and, in return, improves the stability of the cocatalyst. Therefore, it is of great importance to prepare ultrasmall and well-dispersed PdS cocatalyst for photosplitting of $H_2S$.

In this work, we report the highly dispersed PdS anchored as a cocatalyst on $In_2S_3$ of MnS/$In_2S_3$ composite. Introduction of PdS improved the efficiency of photocatalytic hydrogen evolution from $H_2S$ saturated aqueous solution by approximately 6 times, reaching hydrogen evolution rate of 22.7 mmol $g^{-1}$ $h^{-1}$ and an apparent quantum yield (AQY) of 34% at around 395 nm. In particular, the stability of PdS in the system has been confirmed by long-period and cycling experiments. Comprehensive in-depth characterization including scanning transmission electron microscopy (STEM), X-ray photoelectron spectroscopy (XPS) and X-ray absorption spectroscopy (XAS) were carried out to study the nature of Pd species and their interaction with MnS/$In_2S_3$. Pd-In-S bonds were detected in the system and theoretical calculations were furthermore employed to analyze the formation mechanism of the bonds. Finally, photoluminescence (PL) spectroscopy, surface photovoltage (SPV) spectroscopy, photoelectrochemical tests as well as DFT calculations revealed that PdS sites in the composite also facilitate the photogenerated charge separation and the removal of oxidation product, which indicates the potential of noble metal sulfides in sustainable utilization of $H_2S$.

## Experimental

**Materials:** Manganese acetate ($Mn(CH_3COO)_2{\cdot}4H_2O$), indium chloride ($InCl_3{\cdot}4H_2O$), palladium chlorid ($PdCl_2$) are purchased from Aladdin (Shanghai, China). Thioacetamide (TAA) was supplied by Alfa Aesar (Tianjin, China). Sodium sulphide ($Na_2S{\cdot}9H_2O$), hydrochloric acid (HCl) and pyridine ($C_5H_5N$) were purchased from Chron Chemicals (Chengdu, China). All of the materials were used as received without further purification.

**Synthesis of MnS/$In_2S_3$ composite**: MnS/$In_2S_3$ was prepared using the method reported previously.[28] Typically, 1.4 mmol manganese acetate, 0.6 mmol indium chloride and 9.0 mmol thioacetamide were dissolved in 25 mL pyridine to obtain a homogeneous solution with continuous stirring. Then the transparent solution was transferred into a 25 mL Teflon-lined stainless steel autoclave, which was maintained at 180 °C for 30 h. The product was then collected and washed with ethanol under ultrasound. After centrifugation and drying under vacuum at 60 °C overnight, a dark yellow powder was obtained. α-MnS and β-$In_2S_3$ were synthesized using the same technique with only manganese acetate or indium chloride added, respectively.

**Preparation of PdS/MnS/$In_2S_3$ composite**: 200 mg MnS/$In_2S_3$ composite powder was dispersed in 50 mL deionized water with ultrasonic treatment for 0.5 h. Then 3 mL isopropanol and 0.375 mL palladium chloride solution (with a concentration of 8 mg Pd/mL, prepared in 0.57 M HCl solution) were added dropwise to the suspension. After that, the suspension was transferred to a 50 mL glass flask. With continuous stirring and Ar gas flow, the flask was irradiated by a 300 W Xe lamp (full spectrum) for 2 h. Ultimately, the 1.5 wt.% Pd-MnS/$In_2S_3$ composite was collected, washed with ethanol for several times and dried at 60 °C overnight. Here 1.5 wt.% means the weight ratio of introduced Pd to MnS/$In_2S_3$ composite. In this way, MnS/$In_2S_3$ composites loaded with various amounts of Pd precursor were obtained. For convenience, MI-Pd X% (X = 0.2 ~ 2) were used to represent the MnS/$In_2S_3$ composites with different amount of noble metal precursors added during the preparation. As a reference, MI stands for MnS/$In_2S_3$ composite treated in the same way but without addition of the Pd precursor. Fig. S1 shows the photos of MI and MI-Pd 1.5%, noting that the color of sample turned dark yellow from light yellow after introduction of Pd species. Additionally, α-MnS and β-$In_2S_3$ loaded with 1.5 wt.%% Pd were obtained by the same procedure.

**Photocatalytic tests:** The photocatalytic performance tests were conducted using a home-built setup.[28] At first, the system was flushed with Ar. Then 150.0 mL of HCl solution (2.0 mol/L) was added dropwise into 150.0 mL $Na_2S$ solution (1.0mol/L) to produce $H_2S$ gas in 3 - 4 h. The $H_2S$ gas was directly bubbled into a 50 mL flask which contains 50 mL $Na_2S$ (0.1 mol/L) and $Na_2SO_3$ (0.6 mol/L) solution as well as 2.5 mg photocatalyst. Subsequently, the flask was sealed and then irradiated by a 300 W Xe lamp with a cutoff filter (λ > 420 nm). The hydrogen production rate was monitored using a Shimadzu GC-2010 Plus gas chromatograph (GC) (Ar carrier gas, molecular sieve 5 Å columns, TCD detector).

The apparent quantum yield (AQY) of sample was calculated using Eq. 1. The number of incident photon was defined by using monochromatic LED lamps (cf. Table S1).

$$\mathrm{AQY}\ (\%) = \frac{\text{number of reacted electrons}}{\text{number of incident photons}} \times 100\% = \frac{\text{number of hydrogen molecules} \times 2}{\text{number of incident photons}} \times 100\% \quad \text{Eq.1}$$

**Photoelectrochemical tests:** photoelectrochemical tests were carried out on a CHI660E electrochemical workstation (Chenhua Instrument, Shanghai, China) equipped with a standard three-electrode system. The working electrode was prepared by doctor-blade coating method on fluorine doped tin oxide (FTO) with a film thickness of about 50 μm and area of 4 $cm^2$, which was further treated at 200 °C for 3 h in Ar. Pt wire was used as the counter electrode and a saturated calomel electrode (SCE) was the reference electrode. $Na_2SO_3$ solution in water (1.2 mol/L) was used as the electrolyte.

**Characterization:** The crystal structure and crystallinity of the samples were studied by X-ray diffraction (XRD) with Cu Kα radiation using Philips X'Pert diffractometer operated at 40 kV/40 mA. The optical properties were investigated by ultra-violet and visible light (UV-vis) diffuse reflectance spectroscopy (DRS) and photoluminescence (PL) spectroscopy. UV-vis DRS was carried out on a Shimadzu UV-2600 spectrophotometer equipped with an integrating sphere and $BaSO_4$ was used as a

reflectance standard. PL spectra were obtained on a Hitachi F-7000 fluorescence spectrophotometer. Transmission electron microscopy (TEM, Tecnai G2 F30) was used to investigate the morphology and microstructure. High-angle annular dark field (HAADF) images and energy dispersive X-ray spectra (EDS) were recorded on a JEOL ARM200CF with a dual-type EDS detector (JED-2300T) and a FEI titan spherical aberration corrected scanning transmission electron microscope (STEM). X-ray photoelectron spectroscopy (XPS) measurements were performed using a Thermo ESCALAB 250Xi X-ray photoelectron spectrometer using Al Kα radiation and all binding energies were referenced to the C 1s peak at 284.8 eV. The $N_2$ adsorption isotherms and Brunauer-Emmett-Teller (BET) surface areas were determined by the nitrogen adsorption method with Quadrasorb SI. The samples were degassed at 110 °C for 8 h under vacuum before measurements. Surface photovoltage (SPV) measurements were recorded using an Omni - λ 3007 monochromatic-light, including a lock-in amplifier (SR830, Stanford research systems, Inc.), a light chopper and a chamber.

X-ray absorption spectra (XAS) in terms of X-ray absorption near edge structure (XANES) and extended X-ray absorption fine structure (EXAFS) were measured at the CAT end station of the CAT-ACT beamline at the Synchrotron Radiation Source at KIT, Karlsruhe.[45] The samples were measured ex situ at the Pd K absorption edge in transmission mode in form of pellets (53 mg of sample, diameter 5 mm). The beam size was 0.9 mm (vertical) x 1 mm (horizontal). The spectra were normalized and the EXAFS background subtracted and Fourier-transformed (in the k-range 3 – 13.5 $Å^{-1}$) using the ATHENA program from the IFFEFIT software package.[46] XANES spectra were modeled using multiple scattering FEFF 9.6.4. ab initio code.[47] For the PdS spectrum three calculations were performed by using PdS model structure (ICSD collection code 61063) and calculating spectra for all three inequivalent Pd sites. The spectra were then averaged taking into account the corresponding multiplicities. For Pd-doped $In_2S_3$ model, the calculations were conducted only for a tetrahedral site (according to the EXAFS suggesting 4 neighbouring S atoms) in a β-$In_2S_3$ framework (ICSD collection code 202353). For Pd-doped MnS sphalerite, literature-reported model structure (ICSD collection code 76205) doped with nuclear Pd was chosen based on the first shell coordination number 4 and the matching XRD pattern. For the PdS anchored on the surface of $In_2S_3$ and MnS model structures optimized by DFT calculations were used. Radii of the clusters for self-consistent potential calculations (SCF) and for full multiple scattering calculations (FMS) were set as 5 Å. The position of the white line maximum in the theoretical spectra was aligned to the experimental spectra. First shell EXAFS analysis was performed using ARTEMIS (IFFEFIT)[46] and a least square method in R-space (using *k, k², k³*-weighted data) between 1.0 and 2.5 Å. DFT optimized Pd-doped $In_2S_3$ and PdS anchored on $In_2S_3$ were used as model structures and the coordination numbers, interatomic distances, energy shift ($\delta E_0$) and mean square deviation of interatomic distances ($\sigma^2$) were refined. The absolute misfit between theory and experiment was expressed as ρ.

**DFT computational method:** The density functional theory (DFT) calculations were performed using the Materials Studio software, and Cambridge Sequential Total Energy Package (CASTEP)[48] was used for the geometry optimization by the generalized gradient approximation (GGA) with Perdew-Burke-Ernzerhof (PBE) functional.[49, 50] The electron wave functions were expanded using plane waves with a cutoff energy of 300 eV, and the convergence criteria for the residual force and energy on each atom during structure relaxation were set to be 0.05 eV/Å and 2.0 × $10^{-5}$ eV, respectively. A vacuum space of 15 Å was set to separate the interaction with the periodic images. The models which were used for calculation were α-MnS (100) (JCPDS 40 - 1289) and β-$In_2S_3$ (0012) (JCPDS 25 - 0390). The formation energy ($E_{FA}$) of different configurations was calculated as follows:

$$E_{FA} = E_f - E_a - E_b \quad \text{Eq. 2}$$

where $E_f$ was the total energy of final configuration, and $E_a$ and $E_b$ were the energies of separated structures, respectively. The adsorption energies ($E_{AS}$) of sulfur on Pd and PdS were calculated as follows:

$$E_{AS} = E_m - E_{slab} - E_s \quad \text{Eq. 3}$$

where $E_{AS}$ was the total energy of ultimate adsorption configuration, and $E_{slab}$ was the total energy of the clean slab and $E_s$ was the energy of S atom.

## Results and discussion

#### Photocatalytic $H_2$ evolution efficiency from $H_2S$ saturated solution

Pd species were introduced on MnS/$In_2S_3$ (abbreviated as MI) composite by a photodeposition method. Photocatalytic hydrogen evolution from saturated $H_2S$ aqueous solution was then carried out with the as-obtained MI-Pd composite. Fig. 1(a) shows that introduction of Pd species could effectively promote the hydrogen evolution rate of MI, which reaches 22.7 mmol $g^{-1}$ $h^{-1}$ within 5 h at 1.5 wt.% Pd (denoted as MI-Pd 1.5%) under Xe lamp irradiation (λ > 420 nm). Further increase of Pd precursor species to 2 wt.% in the system did not improve the hydrogen evolution efficiency any more, probably due to a possible shielding effect and loss of active sites. AQY of the system was thus measured based on the MI-Pd 1.5% using a series of monochromatic LED light sources (see more information in Table S1). Fig. 1(b) proves that the trends of AQY values under different wavelength matches well with the light absorbance of MI-Pd 1.5%, and this demonstrates that such hydrogen evolution indeed results from the photoexcitation of the composite. A highest AQY value of 34% was obtained at around 395 nm, where the absorbance of MI-Pd 1.5% is also close to the maximum. Moreover, the stability of the system is an important factor for evaluation of the system. As shown in Fig. 1(c), the photocatalytic activity of MI-Pd 1.5% is well maintained during 10 h. Cyclic tests of MI-Pd 1.5% were carried out as well (Fig. 1(d)), which further confirm the stability and obviously improved activity of as-prepared samples in the $H_2S$-

rich system (a comparison of activity reported in this work and in other publications is given in Table S2).

**Structural characterization of MI-Pd**

To shed light on the origins of the activity of MI-Pd, structure and optical properties of the composites were studied. XRD patterns of all MI-Pd samples were similar, with the main reflections indexed to γ-MnS and β-$In_2S_3$ (Fig. 2(a)). No obvious reflections related to any Pd species were observed even if the amount of Pd precursor reaches 2%. This may be attributed to the small size and high dispersion of Pd species. In spite of this, UV-vis DRS indicates that the light absorption in the 450 - 700 nm region slightly increases with the increased amount of introduced Pd species indicating the successful incorporation of Pd species into MI composite. Nevertheless, the exact structure of the Pd species in the system could be barely recognized with the UV-vis DRS data.

Morphology was then studied through TEM and spherical aberration corrected STEM to further explore the micro-structure and the possible Pd species in the composite. In particular, the composite with the highest photocatalytic activity, MI-Pd 1.5%, was deeper investigated. Typically, MI-Pd 1.5 % has a lamellar structure (Fig. 3(a)),[28] which resembles the original MnS/$In_2S_3$ composite. It is worth noting that no extra particles or clusters can be observed on the surface of MI-Pd 1.5 %. Additionally, only two diffraction rings assigned to the (002) facet of γ-MnS and (2212) facet of β-$In_2S_3$ were observed in the selected area electron diffraction (SAED) patterns (Fig. 3(b)), which agrees with the XRD results. In Fig. 3(c), highly resolved lattice fringes were clearly observed for MI-Pd 1.5% in HAADF mode, which were related to the (224) and (1019) facets of β-$In_2S_3$ (Fig. 3(c)). EDS elemental mapping was then used to obtain element distribution in MI-Pd 1.5%. Pd was successfully detected homogeneously distributed in the whole studied area (Fig. 3(d and e)). Meanwhile, Mn, In and S elements were also clearly visible with uniform distribution as a result of the intimate junction of MnS and $In_2S_3$. O was also observed in the measurement, which probably originated from the absorbed water molecules and hydroxyl groups on the surface of the composite. Based on the above data, it is reasonable to judge that ultrasmall and highly dispersed Pd species exist in MI-Pd 1.5%.

Furthermore, the chemical state of the elements in the composite surface was revealed by XPS. Fig. 4 displays the XPS spectra of different elements of MI and MI-Pd 1.5% (see survey spectra in Fig. S2). Distinct signal of Pd could be observed in the MI-Pd 1.5% (Fig. 4(a)). In particular, the fine spectra of Pd exhibit one doublet peak at 337.3 eV and 342.5 eV[51] which corresponds to the 3d 5/2 and 3d 3/2 lines of $Pd^{2+}$, respectively. No signal belonging to $Pd^0$ could be obtained, illustrating absence of elemental Pd. Besides, for the fine spectra of O 1s (Fig. S3(a)), the peak of lattice oxygen at around 530.3 eV, characteristic of oxide,[52] was not detected as well. Hence, the possible existence of PdO in MI-Pd 1.5% was excluded either. Interestingly, we find that, compared to the original MI, the In 3d lines in MI-Pd 1.5% shifted to a higher binding energies, from 444.9 (3d 5/2) and 452.5 (3d 3/2) eV[53] to 445.1 and 452.7 eV, respectively (Fig. 4(b)), while those of Mn 2p remain unchanged (Fig. S3(b)). Such trends are further confirmed by the Mn 2p and In 3d fine spectra of other MI-Pd composites (Fig. S3(b) and Fig. S4(b)). Judging from the electronic state changes of In in MI-Pd 1.5%, the introduced Pd species may have a strong interaction with $In_2S_3$ in the composite. In contrast, the interaction between Pd species and MnS is weak. Binding energy of S 2p also shifted to a higher value from 161.5 (2p 3/2) and 162.7 (2p 1/2) eV to 161.9 and 163.0 eV after addition of Pd species (Fig. 4(c) and S4(c)). Accordingly, we propose that Pd is probably anchored as PdS in the MI-Pd 1.5% composite.

XAS of MI-Pd 1.5% at the Pd K edge were recorded to further verify the existence of PdS. Fig. 5(a) demonstrates that XANES spectrum of Pd in MI-Pd 1.5% differs from that of the reference $Pd^0$ significantly, but strongly resembles that of the reference PdS sample (crystalline PdS from Alfa Aesar, 99% purity). Based on this, existence of $Pd^0$ in MI-Pd 1.5% was further excluded and the chemical nature of Pd species in MI-Pd 1.5% should be very similar to PdS. Here, small differences between the spectra of MI-Pd 1.5% and PdS in the range of 24370-24380 eV may result from the high dispersion of PdS and its possible interaction with MnS/$In_2S_3$ composite. EXAFS spectra of MI-Pd 1.5% are also very similar to the PdS spectrum, in a good agreement with that of the XANES data (Fig. 5(b)). The amplitude of oscillations is almost same, and this means that number of S atoms around Pd in the composite is the same as in PdS (4 nearest neighbors). Furthermore, Fourier-transformed (FT) EXAFS (Fig. 5(c)) reveals that the first coordination shell of Pd (S neighbors, approx. 1.9 Å uncorrected distance) in MI-Pd 1.5% is identical to that of PdS, which again demonstrates that the number of S atoms around Pd and the distance between Pd and S in MI-Pd 1.5% are identical to PdS (Table S3). However, an in-depth examination of the further shells (most notably, the region between 3 - 4 Å, uncorrected for the phase shift) reveals differences between MI-Pd 1.5% and the reference PdS. Therefore, PdS species in MI-Pd possibly have chemical interactions with $In_2S_3$ or MnS in the composite.

Due to very complex geometry of the $In_2S_3$ and MnS models (several overlapping shells at 3 - 4 Å) and the limited number of independent data points in the given range, full EXAFS analysis is unlikely to clearly distinguish the possible interaction between PdS and $In_2S_3$ or MnS. Hence, XANES modeling was employed to identify the structure and location of PdS species in the composites. Here, we used bulk Pd-doped $In_2S_3$ (only tetrahedral site in β-$In_2S_3$ was taken into account), Pd-doped MnS, as well as DFT optimized isolated PdS anchored on the surface of $In_2S_3$ and MnS (in all of which Pd-S bond existed) for the modeling, and the calculated XANES spectra are compared against the experimental ones (Fig. 5(a and d) and Fig. S5). Typically, XANES modeling does not reproduce absolute energies reliably; however, relative positions of the spectral features are well reproduced. The results show that the relative peak positions and the shape of the experimental spectrum of MI-Pd 1.5% are closer to the theoretical spectra of the Pd-doped $In_2S_3$ model or PdS anchored on $In_2S_3$ surface, rather than that of Pd-doped MnS. Consequently, PdS species

in MI-Pd 1.5% should mainly interact with $In_2S_3$ instead of MnS. This conclusion is supported by the XPS data.

XPS and EXAFS data bring forward that the model of PdS anchored on $In_2S_3$ surface results in a good fit to the experimental spectrum (Table S3 and Fig. S6). Such a result was further supported by DFT calculations (Table S4 and Fig. S7). The formation energy of Pd-S-In bond at the interface between PdS and $In_2S_3$ is much more negative (-4.9 eV for on octahedral site and -4.5 eV for tetrahedral site) than that of the Pd-doped $In_2S_3$ (1.1 eV). Accordingly, PdS loaded on $In_2S_3$ with bridged S atoms is more stable, and it should be the most likely structure in MI-Pd composites.

To figure out why the interaction between PdS and $In_2S_3$ is dominant in the composite, DFT calculations were further utilized to analyze the structure stability of PdS bonded with $In_2S_3$ or MnS. We find that the formation energy of the PdS-$In_2S_3$ composite is more negative (-4.9 eV, Fig. 6(a) and Table S4) than that of the PdS-MnS (-4.1 eV, Fig. 6(b) and Table S4); therefore, the anchoring of PdS on $In_2S_3$ in MnS/$In_2S_3$ is thermodynamically preferable.

Moreover, to evaluate whether the interaction between PdS and $In_2S_3$ is more advantageous for the photocatalytic activity than the PdS and MnS interaction, PdS were separately loaded on MnS and $In_2S_3$. Thus, the influence of PdS on different substances in $H_2S$ splitting was explored. As shown in Fig. 6(c), without MnS/$In_2S_3$ heterojunction, the photocatalytic performance of MnS or $In_2S_3$ has decreased a lot. Importantly, introduction of PdS could promote hydrogen evolution efficiency of the pristine $In_2S_3$ by approximately 10 times, while it only promotes that of the pristine MnS by approximately 2 times. As a result, preferable interaction between PdS and $In_2S_3$ could make the positive influence of PdS reach the largest extent in MI-Pd composites.

Moreover, the preferable anchoring of PdS on $In_2S_3$ is also favored when considering the charge separation in MnS/$In_2S_3$. As MnS/$In_2S_3$ is Z-Scheme heterojunction and photogenerated holes are collected on the $In_2S_3$ side,[28] the photogenerated holes in the composite should be largely transferred to PdS due to the close interaction between PdS and $In_2S_3$. PdS is widely reported to facilitate hole transfer from metal sulfides to the environment,[54] hence, with the preferable anchoring of PdS on $In_2S_3$, holes could be effectively transferred by PdS during the reaction. In addition, the strong chemical interaction between PdS and $In_2S_3$ could also strengthen the anchoring of PdS and prevent its detachment from the MI substrate, which could enhance the stability of the system. It could also endow high PdS dispersion on MI, which increases the number of active sites available for catalysis.[55-58]

**Significance of PdS in MI-Pd for photocatalysis**

In order to investigate the mechanism of promotion of photocatalytic splitting of $H_2S$ by PdS in MI-Pd, a thorough physico-chemical characterization of MI-Pd 1.5% and MI was performed. BET surface area analysis was first carried out to check the possible surface area changes of the two samples (Fig. S8 and Table S5). It turns out that the surface area of MI-Pd 1.5% (32 $m^2 g^{-1}$) is a little smaller than that of MI (39 $m^2 g^{-1}$); therefore, the surface area change with PdS is not the main factor contributing to the improvement activity in MI-Pd. The PL spectra of MI and MI-Pd 1.5% were then recorded. Fig. 7(a) illustrates that PL intensity of MI has obviously decreased in MI-Pd. This reflects the decreased possibility of radiative charge recombination and it is often indicative of promoted charge transfer efficiency of the system in photocatalysis. Such speculation was further supported by SPV measurements (Fig. 7(b)). Compared with pristine MI, the PdS containing sample displays a much higher photovoltage in the whole measured wavelength range, with a maximum value located at near 390 nm. Additionally, transient photocurrent response of MI-Pd 1.5% is more evident than that of MI (Fig. 7(c)) and the charge transfer resistance of the MI-Pd 1.5% obtained from the electrochemical impedance spectra (EIS) is smaller than that of the MI (Fig. 7(d)). Hence, these data altogether provide compelling evidence that PdS in MI-Pd could remarkably improve charge separation efficiency of the MnS/$In_2S_3$ composite.

As surface reaction dynamics is also an important factor influencing the photocatalytic efficiency, the rate of desorption of the initial oxidation product, in particular elemental sulfur, in our system, would also affect the photocatalytic activity of the composite.[59] Accordingly, calculations based on DFT with CASTEP were performed to compare the adsorption energy (AE) of sulfur on PdS with that on the traditional metal cocatalyst Pd (Fig. S9). The results (Table S6) revealed that AE of S on PdS (-3.7 eV) is smaller than that on Pd (-5.5 eV); conversely, desorption of oxidation product sulfur from PdS should be easier than that from Pd. Consequently, introduction of PdS could facilitate the desorption of sulfur to some extent, which ultimately promotes the photocatalytic efficiency of the system as well.

**Structure stability of MI-Pd after photocatalysis**

As mentioned before, stability is an essential criterion for evaluation of photocatalysts, especially in $H_2S$ rich systems. For this reason, the structure of MI-Pd was characterized after photocatalysis. XRD data manifests that the major diffraction peaks of the original MI-Pd (Fig. S10) remain unchanged. Moreover, TEM results of MI-Pd 1.5% after photocatalysis show that the lamellar structure of MI-Pd is well preserved, and the diffraction rings (Fig. S11(b)) as well as the exposed lattice planes (Fig. S11(c) and S11(d)) from MnS and $In_2S_3$ are still discernable. The results demonstrate the structure stability of MI-Pd 1.5% during photocatalysis. Notably, in the XRD pattern, other than original diffraction peaks from MI-Pd, weak peaks related to elemental sulfur emerge. This suggests that sulfur is one of the final oxidation products in our system. Furthermore, XPS shows a very similar result: all the fine spectra of Mn, In and Pd in the MI-Pd 1.5% after photocatalysis remain (Fig. S12) the same, while that of S 2p displays a new signal assigned to $S^0$. As for Pd species in the composite, XANES and $k^2$-weighted EXAFS spectra of Pd from MI-Pd 1.5% before and after photocatalysis (Fig. S13) are identical, suggesting the

stable coordination environment of Pd in our sample. Based on these results, photocorrosion of the present sulfide composite MI-Pd is largely suppressed. It has been reported that PdS is beneficial for hole transfer in photocatalysis;[54] in our system, it could facilitate the transfer of photogenerated holes from $MnS/In_2S_3$ to the reaction medium, which in return protects $MnS/In_2S_3$ from self-oxidation, and finally enhances the long-term and cycle photostability of MI-Pd 1.5%. Moreover, the high dispersion of PdS and its chemical interaction with $In_2S_3$ in the composite may further guarantee its stability.

## Conclusion

In summary, for green utilization of highly toxic $H_2S$, $MnS/In_2S_3$ composite loaded with ultrasmall and highly dispersed PdS was proven to be an effective photocatalyst capable of generating hydrogen. Introduction of PdS in the $MnS/In_2S_3$ composite significantly increases the hydrogen production rate of the system to 22.7 mmol $g^{-1}$ $h^{-1}$, with a maximum AQE of 34% at around 395 nm. Though XRD and TEM results present no strong signal of PdS in MI-Pd, detailed analysis of STEM and XPS together with XAS clearly shows the existence of well-dispersed PdS. Additionally, strong interaction has been confirmed between PdS and $In_2S_3$ through Pd-S-In bonds on the interface of PdS and $In_2S_3$. These phenomena are highly related to the recent single-atom related works which revealed chemical interaction of substance and substrate to ensure maximum utilization of noble metal in photocatalysis. Moreover, the preferable decoration of PdS on $In_2S_3$ in $MnS/In_2S_3$ could stabilize surface PdS and remarkably promote the activity. Charge separation efficiency and surface reaction kinetics was promoted in the presence of PdS; and stability of MI-Pd during photocatalysis is well preserved. This work has shown innovative introduction of ultrasmall and highly dispersed PdS on $In_2S_3$ of $MnS/In_2S_3$ for photocatalytic splitting of $H_2S$, and moreover it has demonstrated the importance of the preferable anchoring of PdS on the binary $MnS/In_2S_3$ composite for efficiency enhancement, which could be further extended to a series of other photocatalysts in the future.

## Conflicts of interest

There are no conflicts to declare.

## Acknowledgements

This research was financially supported by National Natural Science Foundation of China (U1862111 and U1232119), Sichuan Provincial International Cooperation Project (2017HH0030), the Innovative Research Team of Sichuan Province (2016TD0011). We thank the Synchrotron Radiation Source at KIT, Karlsruhe, for providing beam time, KIT for supporting the catalysis infrastructure at the CAT beamline, and beamline scientists Dr. Anna Zimina and Dr. Tim Pruessmann at CAT-ACT for the support during measurements.

## References

1. R. O. Beauchamp, J. S. Bus, J. A. Popp, C. J. Boreiko, D. A. Andjelkovich and P. Leber, *CRC Crit. Rev. Toxicol.*, 1984, **13**, 25-97.
2. N. P. Dasgupta, J. F. Mack, M. C. Langston, A. Bousetta and F. B. Prinz, *Rev. Sci. Instrum.*, 2010, **81**, 044102.
3. I. A. Gargurevich, *Ind. Eng. Chem. Res.*, 2005, **44**, 7706-7729.
4. M. Lashgari and M. Ghanimati, *Chem. Eng. J.*, 2019, **358**, 153-159.
5. A. PiÉPlu, O. Saur, J.-C. Lavalley, O. Legendre and C. NÉDez, *Catal. Rev.*, 1998, **40**, 409-450.
6. X. Zong, J. Han, B. Seger, H. Chen, G. Lu, C. Li and L. Wang, *Angew. Chem. Int. Ed.*, 2014, **53**, 4399-4403.
7. W. Ma, J. Han, W. Yu, D. Yang, H. Wang, X. Zong and C. Li, *ACS Catal.*, 2016, **6**, 6198-6206.
8. K. Polychronopoulou, F. Cabello Galisteo, M. López Granados, J. L. G. Fierro, T. Bakas and A. M. Efstathiou, *J. Catal.*, 2005, **236**, 205-220.
9. C. A. Linkous, C. Huang and J. R. Fowler, *J. Photochem. Photobiol., A*, 2004, **168**, 153-160.
10. L. Zhang, P. De Schryver, B. De Gusseme, W. De Muynck, N. Boon and W. Verstraete, *Water Res.*, 2008, **42**, 1-12.
11. M. Lashgari and M. Ghanimati, *J. Hazard. Mater.*, 2018, **345**, 10-17.
12. G. Ma, H. Yan, J. Shi, X. Zong, Z. Lei and C. Li, *J. Catal.*, 2008, **260**, 134-140.
13. A. Prakash, M. Dan, S. Yu, S. Wei, Y. Li, F. Wang and Y. Zhou, *Sol. Energy Mater. Sol. Cells*, 2018, **180**, 205-212.
14. J. Zhu, S. Wang, Z. Bian, S. Xie, C. Cai, J. Wang, H. Yang and H. Li, *CrystEngComm*, 2010, **12**, 2219-2224.
15. W. He, Y. Sun, G. Jiang, Y. Li, X. Zhang, Y. Zhang, Y. Zhou and F. Dong, *Appl. Catal., B*, 2018, **239**, 619-627.
16. W. Cui, J. Li, Y. Sun, H. Wang, G. Jiang, S. C. Lee and F. Dong, *Appl. Catal., B*, 2018, **237**, 938-946.
17. W. Cui, J. Li, F. Dong, Y. Sun, G. Jiang, W. Cen, S. C. Lee and Z. Wu, *Environ. Sci. Technol.*, 2017, **51**, 10682-10690.
18. H. Yoshida, L. Zhang, M. Sato, T. Morikawa, T. Kajino, T. Sekito, S. Matsumoto and H. Hirata, *Catal. Today*, 2015, **251**, 132-139.
19. M. Yamamoto, T. Yoshida, N. Yamamoto, T. Nomoto, Y. Yamamoto, S. Yagi and H. Yoshida, *J. Mater. Chem. A*, 2015, **3**, 16810-16816.
20. U. V. Kawade, R. P. Panmand, Y. A. Sethi, M. V. Kulkarni, S. K. Apte, S. D. Naik and B. B. Kale, *RSC Adv.*, 2014, **4**, 49295-49302.
21. Y. Fang, Z. Li, Y. Jiang, X. Wang, H.-Y. Chen, N. Tao and W. Wang, *Proc. Natl. Acad. Sci. U. S. A.*, 2017, **114**, 10566-10571.
22. M. Dan, A. Prakash, Q. Cai, J. Xiang, Y. Ye, Y. Li, S. Yu, Y. Lin and Y. Zhou, *Sol. RRL*, 2019, **3**, 1800237.
23. X.-B. Fan, S. Yu, H.-L. Wu, Z.-J. Li, Y.-J. Gao, X.-B. Li, L.-P. Zhang, C.-H. Tung and L.-Z. Wu, *J. Mater. Chem. A*, 2018, **6**, 16328-16332.
24. L. Cheng, Q. Xiang, Y. Liao and H. Zhang, *Energy Environ. Sci.*, 2018, **11**, 1362-1391.
25. S. Yu, X.-B. Fan, X. Wang, J. Li, Q. Zhang, A. Xia, S. Wei, L.-Z. Wu, Y. Zhou and G. R. Patzke, *Nat. Commun.*, 2018, **9**, 4009.
26. X.-B. Fan, S. Yu, F. Zhan, Z.-J. Li, Y.-J. Gao, X.-B. Li, L.-P. Zhang, Y. Tao, C.-H. Tung and L.-Z. Wu, *ChemSusChem*, 2017, **10**, 4833-4838.
27. M. Dan, Q. Zhang, Y. Zhong and Y. Zhou, *J. Inorg. Mater.*, 2017, **32**, 1308-1314.
28. M. Dan, Q. Zhang, S. Yu, A. Prakash, Y. Lin and Y. Zhou, *Appl. Catal., B*, 2017, **217**, 530-539.
29. Z. H. N. Al-Azri, W.-T. Chen, A. Chan, V. Jovic, T. Ina, H. Idriss and G. I. N. Waterhouse, *J. Catal.*, 2015, **329**, 355-367.

30. B. Li, L. Shao, R. Wang, X. Dong, F. Zhao, P. Gao and Z. Li, *J. Mater. Chem. A*, 2018, **6**, 6344-6355.
31. X. Pan and Y.-J. Xu, *J. Phys. Chem. C*, 2013, **117**, 17996-18005.
32. A. B. Ijzermans, *Recl. Trav. Chim. Pays-Bas*, 1969, **88**, 334-343.
33. A. B. Ijzermans, *Recl. Trav. Chim. Pays-Bas*, 1969, **88**, 344-352.
34. T. Kako, H. Irie and K. Hashimoto, *J. Photochem. Photobiol., A*, 2005, **171**, 131-135.
35. J. Yang, H. Yan, X. Wang, F. Wen, Z. Wang, D. Fan, J. Shi and C. Li, *J. Catal.*, 2012, **290**, 151-157.
36. J. Song, H. Zhao, R. Sun, X. Li and D. Sun, *Energy Environ. Sci.*, 2017, **10**, 225-235.
37. C. Ye , M. D. Regulacio , S. H. Lim, S. Li, Q.-H. Xu and M.-Y. Han, *Chem. - Eur. J.*, 2015, **21**, 9514-9519.
38. A. Uzun and B. C. Gates, *J. Am. Chem. Soc.*, 2009, **131**, 15887-15894.
39. J. O. Ehresmann, P. W. Kletnieks, A. Liang, V. A. Bhirud, O. P. Bagatchenko, E. J. Lee, M. Klaric, B. C. Gates and J. F. Haw, *Angew. Chem. Int. Ed.*, 2006, **45**, 574-576.
40. A. Wang, J. Li and T. Zhang, *Nat. Rev. Chem.*, 2018, **2**, 65-81.
41. B. Qiao, A. Wang, X. Yang, L. F. Allard, Z. Jiang, Y. Cui, J. Liu, J. Li and T. Zhang, *Nat. Chem.*, 2011, **3**, 634-641.
42. H. Zhang, G. Liu, L. Shi and J. Ye, *Adv. Energy Mater.*, 2017, **8**, 1701343.
43. X. Wu, H. Zhang, J. Dong, M. Qiu, J. Kong, Y. Zhang, Y. Li, G. Xu, J. Zhang and J. Ye, *Nano Energy*, 2018, **45**, 109-117.
44. P. Liu, Y. Zhao, R. Qin, S. Mo, G. Chen, L. Gu, D. M. Chevrier, P. Zhang, Q. Guo, D. Zang, B. Wu, G. Fu and N. Zheng, *Science*, 2016, **352**, 797-801.
45. A. Zimina, K. Dardenne, M. A. Denecke, D. E. Doronkin, E. Huttel, H. Lichtenberg, S. Mangold, T. Pruessmann, J. Rothe, T. Spangenberg, R. Steininger, T. Vitova, H. Geckeis and J. D. Grunwaldt, *Rev. Sci. Instrum.*, 2017, **88**, 113113-113129.
46. B. Ravel and M. Newville, *J. Synchrotron Radiat.*, 2005, **12**, 537-541.
47. J. J. Rehr, J. J. Kas, F. D. Vila, M. P. Prange and K. Jorissen, *Phys. Chem. Chem. Phys.*, 2010, **12**, 5503-5513.
48. S. Wei, F. Wang, M. Dan, K. Zeng and Y. Zhou, *Appl. Surf. Sci.*, 2017, **422**, 990-996.
49. S. Sinthika, E. M. Kumar and R. Thapa, *J. Mater. Chem. A*, 2014, **2**, 12812-12820.
50. P. Li, F. Wang, S. Wei, X. Li and Y. Zhou, *Phys. Chem. Chem. Phys.*, 2017, **19**, 4405-4410.
51. R. Bhatt, S. Bhattacharya, R. Basu, A. Singh, U. Deshpande, C. Surger, S. Basu, D. K. Aswal and S. K. Gupta, *Thin Solid Films*, 2013, **539**, 41-46.
52. L. Ouyang, P.-f. Tian, G.-j. Da, X.-C. Xu, C. Ao, T.-y. Chen, R. Si, J. Xu and Y.-F. Han, *J. Catal.*, 2015, **321**, 70-80.
53. Y. Li, G. Chen, Q. Wang, X. Wang, A. Zhou and Z. Shen, *Adv. Funct. Mater.*, 2010, **20**, 3390-3398.
54. H. Yan, J. Yang, G. Ma, G. Wu, X. Zong, Z. Lei, J. Shi and C. Li, *J. Catal.*, 2009, **266**, 165-168.
55. X. Zhang, J. Guo, P. Guan, C. Liu, H. Huang, F. Xue, X. Dong, S. J. Pennycook and M. F. Chisholm, *Nat. Commun.*, 2013, **4**, 1924.
56. P. Yin, T. Yao, Y. Wu, L. Zheng, Y. Lin, W. Liu, H. Ju, J. Zhu, X. Hong, Z. Deng, G. Zhou, S. Wei and Y. Li, *Angew. Chem. Int. Ed.*, 2016, **55**, 10800-10805.
57. H. Yan, H. Cheng, H. Yi, Y. Lin, T. Yao, C. Wang, J. Li, S. Wei and J. Lu, *J. Am. Chem. Soc.*, 2015, **137**, 10484-10487.
58. J. Xing, J. F. Chen, Y. H. Li, W. T. Yuan, Y. Zhou, L. R. Zheng, H. F. Wang, P. Hu, Y. Wang, H. J. Zhao, Y. Wang and H. G. Yang, *Chem. - Eur. J.*, 2014, **20**, 2138-2144.
59. M. Dan, S. Wei, D. E. Doronkin, Y. Li, Z. Zhao, S. Yu, J.-D. Grunwaldt, Y. Lin and Y. Zhou, *Appl. Catal., B*, 2019, **243**, 790-800.

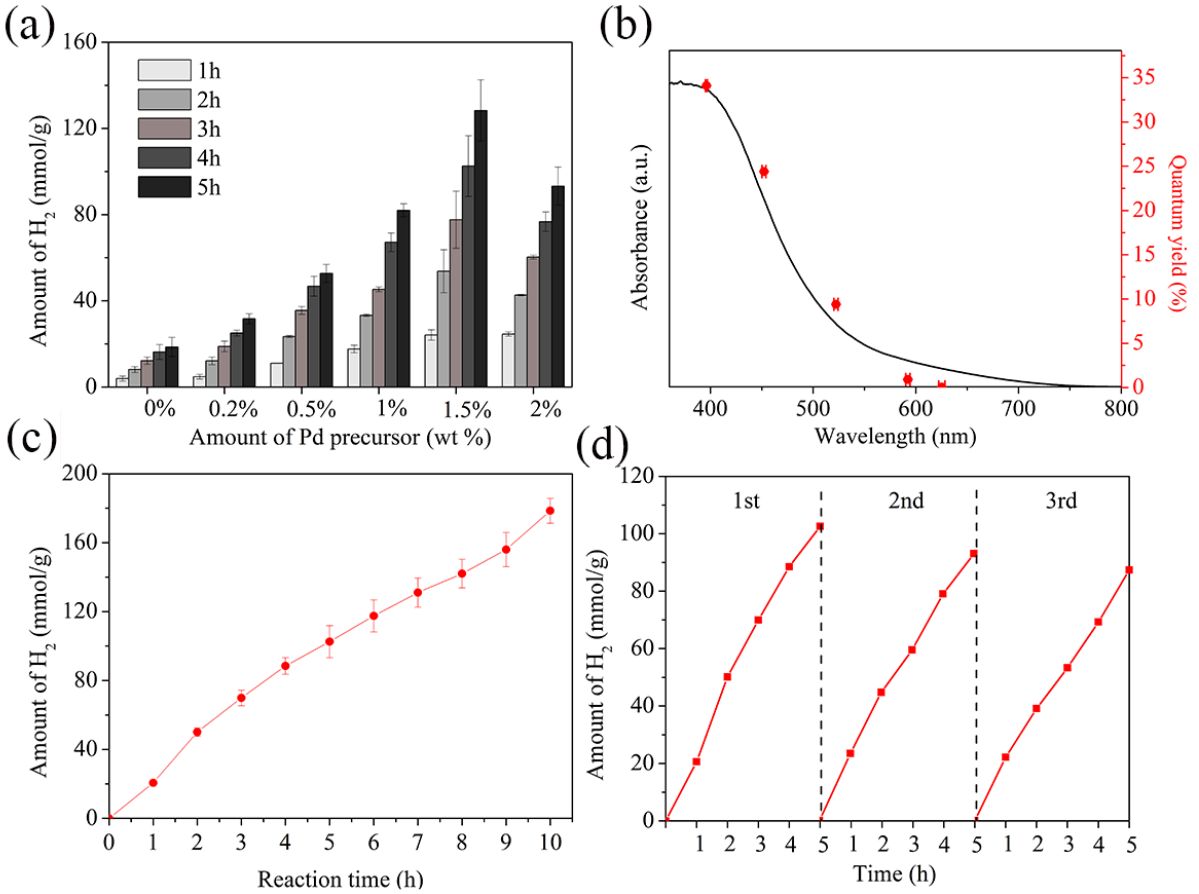


**Fig.1** Photocatalytic hydrogen production rate of MI, and MI-Pd X % (X = 0.2 ~ 2) (a); ultra-violet and visible light diffuse reflectance spectra and apparent quantum yield at different wavelength of MI-Pd 1.5 % (b); 10 h long period photocatalytic hydrogen production rate of MI-Pd 1.5 % (c); three rounds cyclic photocatalytic hydrogen production rate of MI-Pd 1.5 % (d)

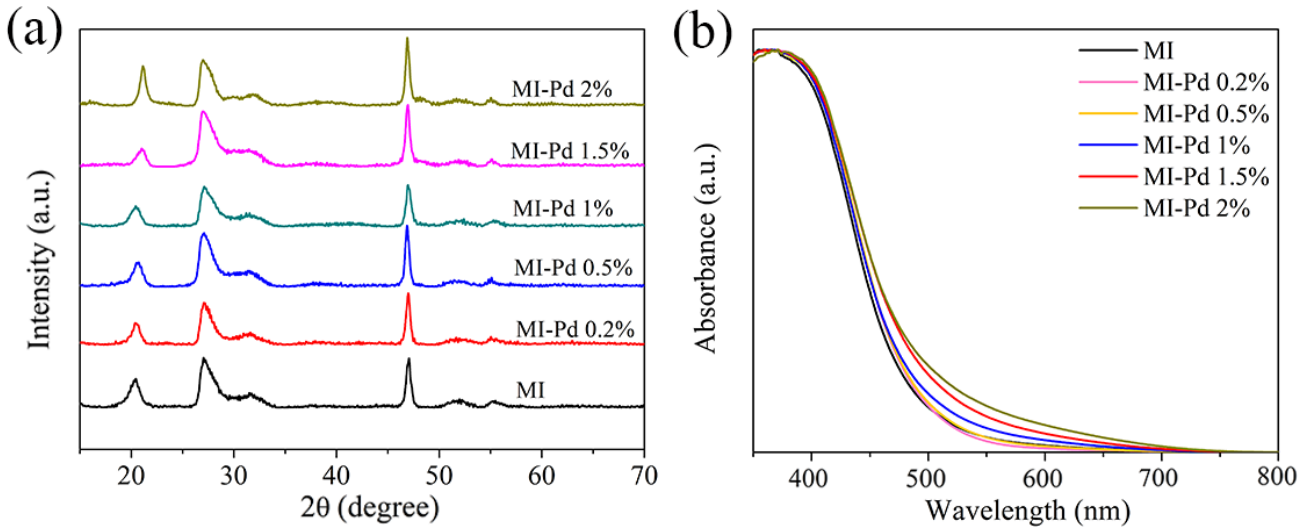


**Fig.2** X-ray diffraction pattern (a) and ultra-violet and visible light diffuse reflectance spectra (b) of MI, and MI-Pd X% (X = 0.2 ~ 2)

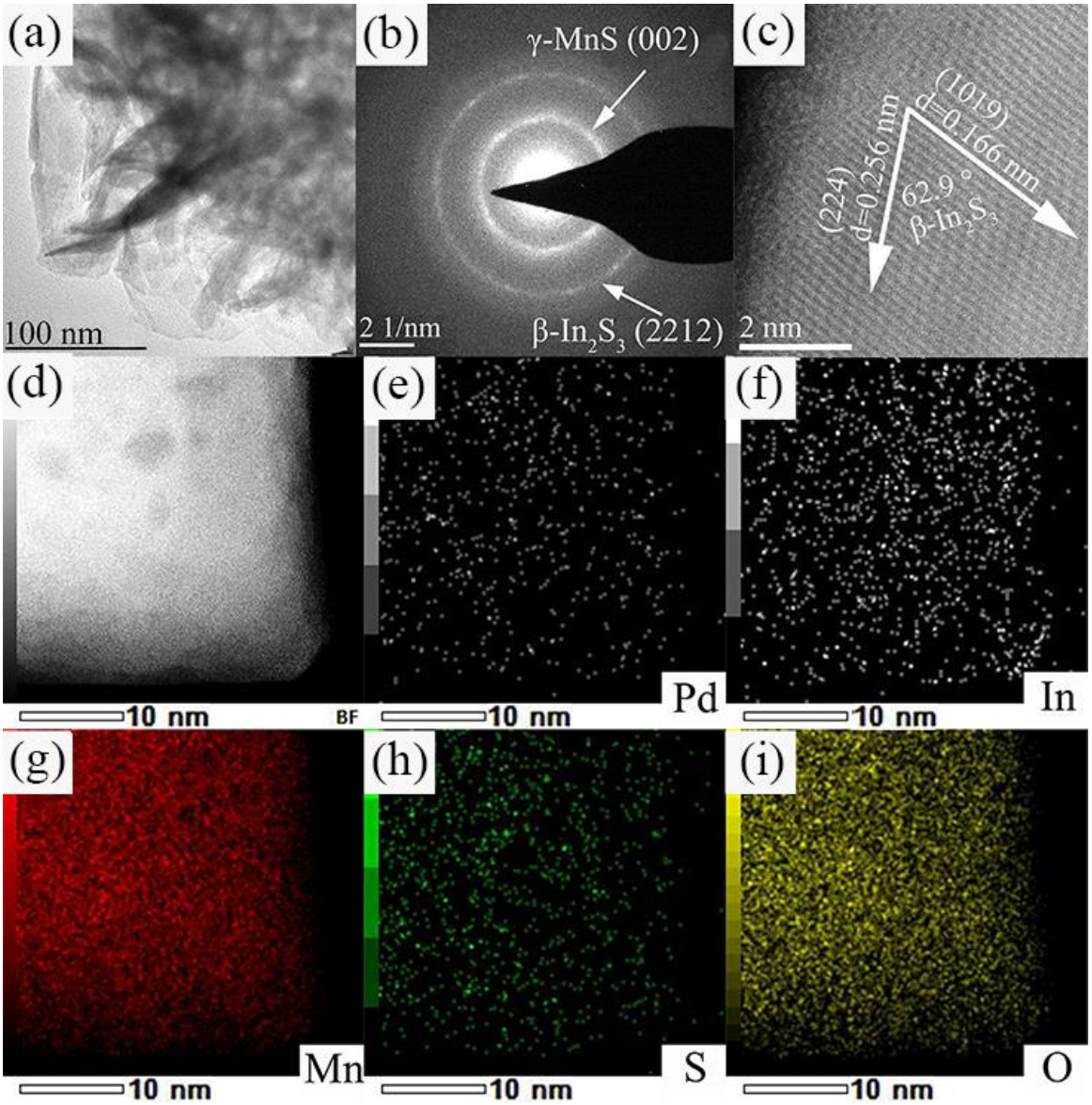


**Fig. 3** Transmission electron microscope image (a), selected area electron diffraction (beam diameter: 200 nm) image (b), spherical aberration corrected scanning transmission electron microscope atomic resolution high-angle annular dark-field image (c), and energy dispersive X-ray spectrum element maps - selected area (d), element Pd (e), element In (f), element Mn (g), element S (h), element O (i) of MI-Pd 1.5%

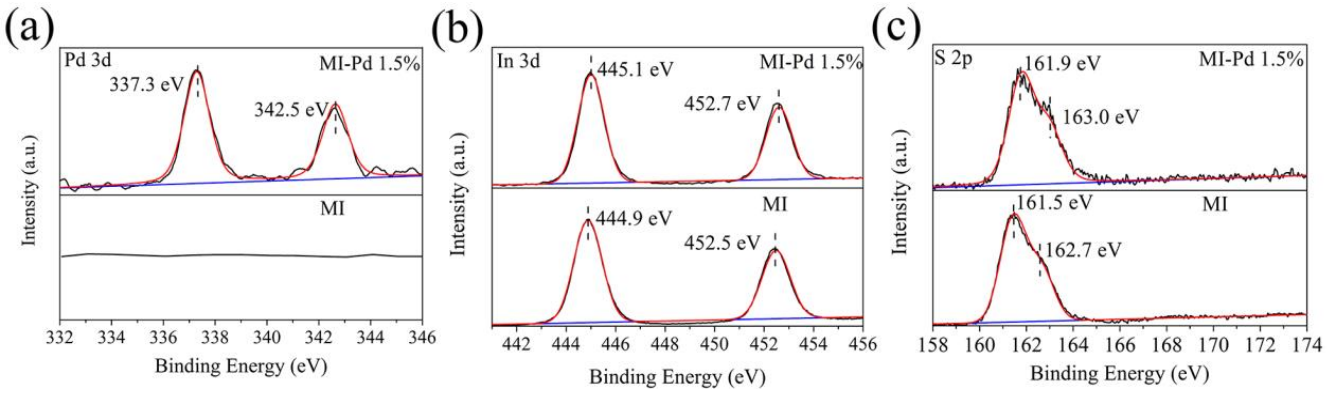


**Fig. 4** X-ray photoelectron fine spectra Pd 3d (a), In 3d (b), and S 2p (c) of MI, and MI-Pd 1.5%

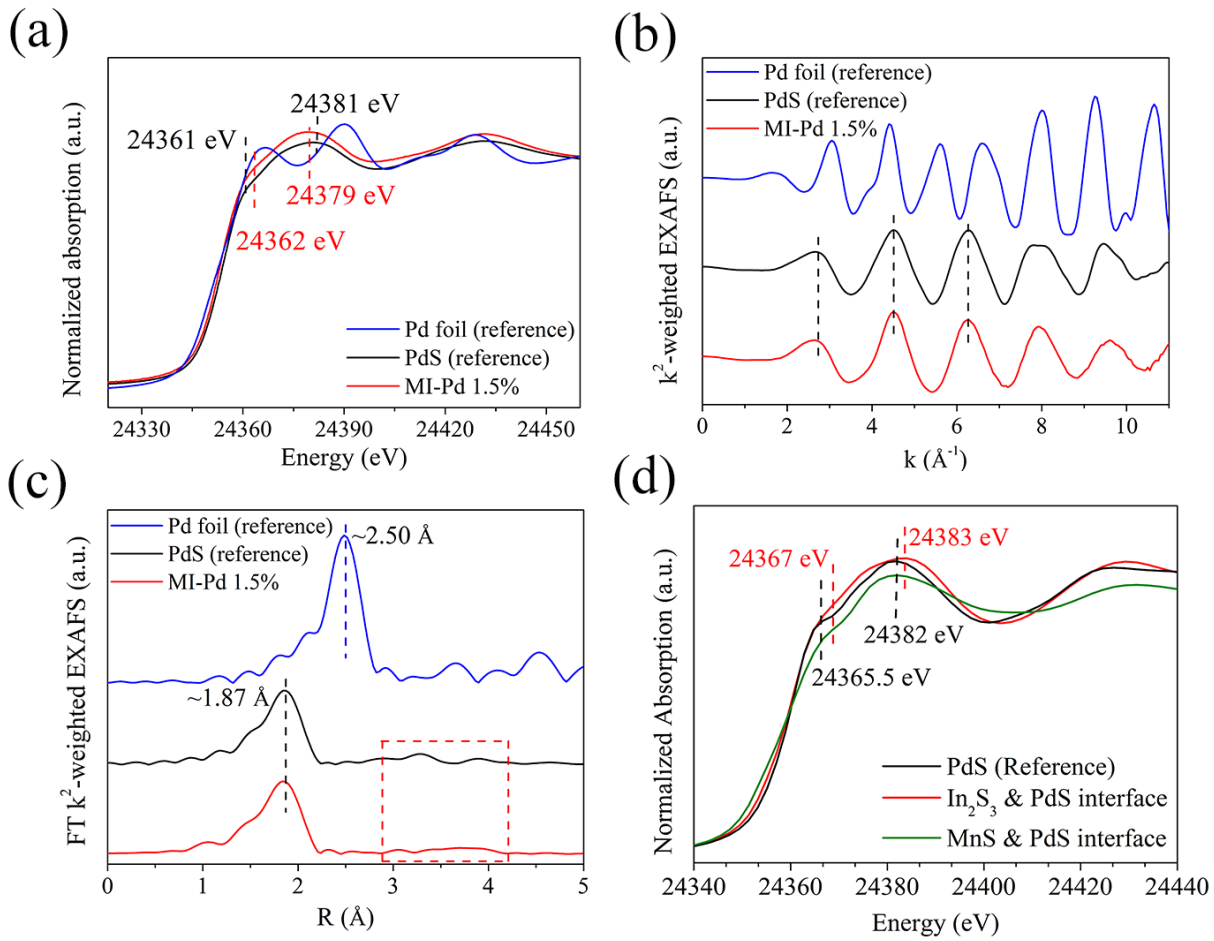


**Fig. 5** Normalized X-ray absorption near edge spectra (a), $k^2$-weighted extended X-ray absorption fine spectra (b), and Fourier-transformed $k^2$-weighted extended X-ray absorption fine spectra (c) of MI-Pd 1.5% (fresh), Pd foil reference and PdS reference; theoretical X-ray absorption near edge spectra (d) of $In_2S_3$ & PdS interface, MnS & PdS interface and PdS reference

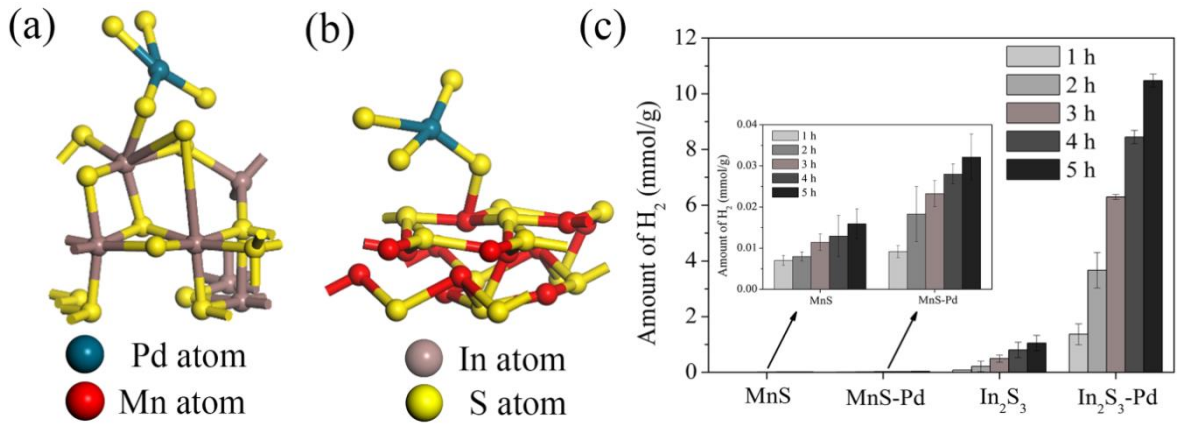


**Fig. 6** The model structures of $In_2S_3$ & PdS interface (a) and MnS & PdS interface (b); photocatalytic hydrogen production over MnS, MnS-Pd, $In_2S_3$, and $In_2S_3$-Pd with in 5 h. (The added Pd precursor amount is 1.5% which is consistent with MI-Pd 1.5%)(c)

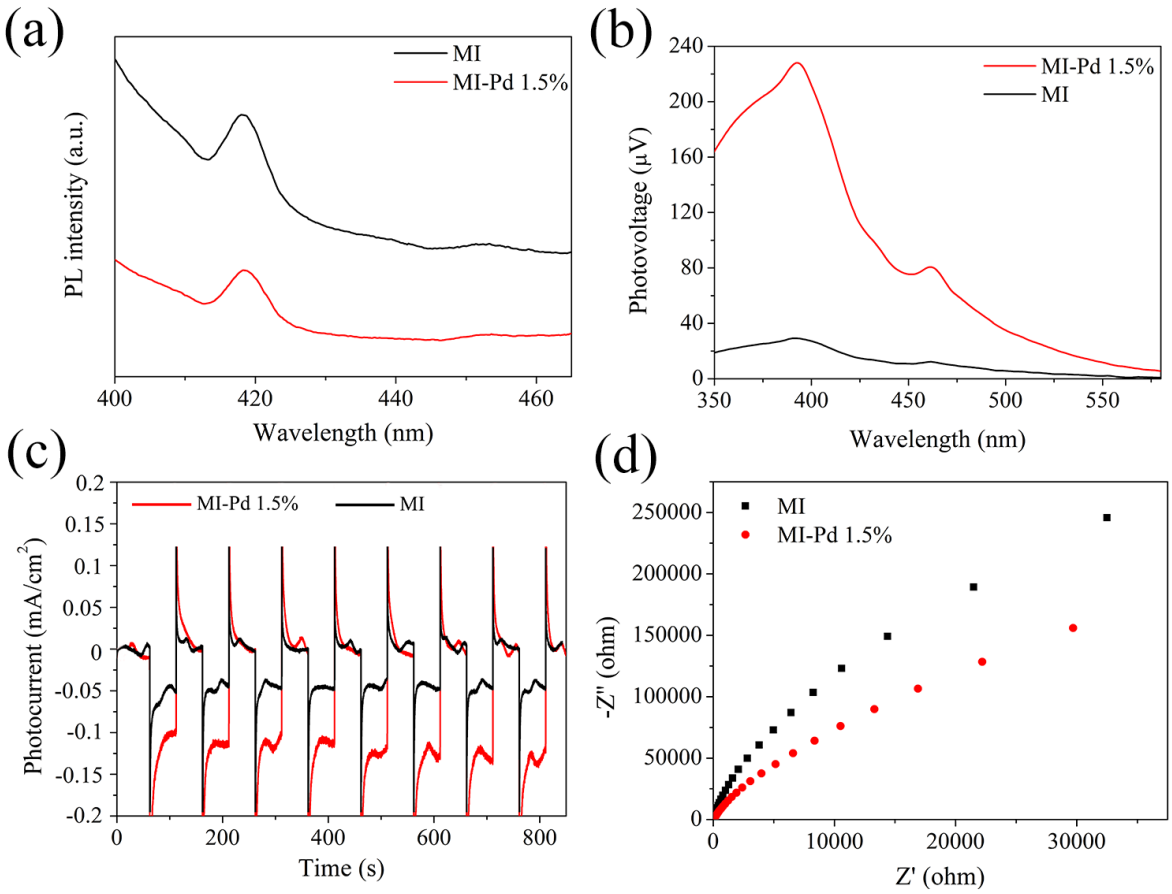


**Fig. 7** Photoluminescence spectra (a), surface photovoltage spectra (b), transient photocurrent response test (c), and electrochemical impedance spectra (d) of MI and MI-Pd 1.5%